Supporting information

Robust thermoelectric module based on $MgAgSb/Mg_3(Sb,Bi)_2$ with an 8.5% conversion efficiency and a 72 K maximum cooling

Pingjun Ying[1], Lennart Wilkens[1], Heiko Reith[1], Nicolas Perez Rodriguez[1], Xiaochen Hong[1,2] Qiongqiong Lu[1], Christian Hess[1,2], Kornelius Nielsch[1,3,4]*, Ran He[1,*]

[1]*Leibniz Institute of Solid State and Materials Science, 01069 Dresden, Germany*

[2]*School of Mathematics and Natural Sciences, University of Wuppertal, 42079, Wuppertal, Germany*

[3]*Institute of Materials Science, Technische Universität Dresden, 01062 Dresden, Germany*

[4]*Institute of Applied Physics, Technische Universität Dresden, 01062 Dresden, Germany*

I. Methods

Synthesis of n- and p-type materials with/without contacts

We prepare *n*-type $Mg_{3+\delta}Y_xSb_{0.6}Bi_{1.4}$ (δ=0.2 or 0.6, x=0.001, 0.002, 0.003, 0.004, and 0.005) and *p*-type $MgAg_{0.97}Sb_{0.99}$ compounds through mechanical alloying. High-purity elements Bi (granules, 99.99%, Alfa Aesar), Sb (rod, 99.999%, Alfa Aesar), Y (pieces, 99.9%, Alfa Aesar), Mg (turning, 99.98%, Alfa Aesar), and Ag (powder, 99.9%, HMW Hauner) are weighed out according to the stoichiometry with a total mass of 10 grams. For each sample, the weighed elements are loaded into a hardened steel ball-milling jar in a glove box under an argon atmosphere with an oxygen and water level below 1.0 ppm and then ball-milled with two ϕ12 mm stainless-steel balls using a SPEX 8000D machine. The *p*-type compounds are milled using a two-step method as suggested by Zhao, *et al*[1]. The n-type compounds are milled for 10 hours with powder loosing on the 5th hour. The ball-milled powder and a contact powder are then loaded into a sintering die with an inner diameter of 20.0 mm in a glove box. The as prepared powders are sintered by field-assisted sintering (FAST, FCT System GmbH). A graphite die is used to sinter the *n*-type $Mg_{3.6}Y_xSb_{0.6}Bi_{1.4}$ under varied temperatures (973 K, 1023 K, and 1073 K) and 50 MPa for 3 min. A tungsten carbide (WC) die is used to sinter the *p*-type $MgAg_{0.97}Sb_{0.99}$ under 553 K and 120 MPa for 5 min. For contacting making, pure powder Fe (99.8%) and Ag (99.9%) are loaded into the dies as the contact layers to realize low contact resistance, and the thermoelectric powder is sandwiched between 2 layers of contact powders. The entire sintering is carried out under vacuum.

Sample characterization and measurement

Room-temperature X-ray diffraction patterns are measured in a Bruker D8 Advance diffractometer (Co radiation) to characterize the phases. A scanning electron microscope (SEM) is applied to characterize the morphology of sample surfaces that are freshly broken, and an Energy-dispersive X-ray spectroscopy (EDX) is applied to map the elemental distribution across the junctions between the TE materials and the contact layers. The sintered compounds are cut and polished to the desired sizes for thermoelectric transport measurement. The electrical resistivity (ρ) and the Seebeck coefficient (S) are measured using a commercial device LSR-3 (Linseis). The thermal conductivity (κ) is calculated as a multiplication of thermal diffusivity (D), specific heat (c_P), and mass density (d). The thermal diffusivity and the mass density are measured by commercial laserflash devices (LFA1000, Linseis; LFA457, Netzsch) and an Archimedes kit, respectively. The specific heat takes the literature value of Agne, *et al*[2]. Hall concentration (n_H) are measured by an HCS-1 high temperature Hall setup (Linseis) from

300 K to 473 K in an Ar-protected environments using the Van der Pauw method. Magnetic inductions of +0.67 T and -0.61 T are applied by permanent magnets. To achieve high quality Hall data, the sample thickness is reduced to ~0.2 mm and below. To justify Hall measurement result, we also applied a physical property measurement system (PPMS, Quantum Design) using the Hall-bar method under a ±9 T magnetic induction at room temperature. The Hall mobility (μ_H) is calculated as $\mu_H = 1/\rho n_H e$. The measurement errors are 4%, 5%, and 12% for the electrical resistivity, Seebeck coefficient, and thermal conductivity, respectively. Explicitly, the uncertainties of thermal conductivity originate from 2% in mass density, 4% in diffusivity, and 6% in specific heat. Therefore, the uncertainties in power factor and zT are 10% and 20%, respectively. To increase the readability of the graphs, we do not add the error bars on the curves.

Thermoelectric module fabrication and characterization

The sintered *n*- and *p*-type wafers with contact layers are cut into 4.0 × 4.0 × 7.9 mm^3 pieces using a diamond wire saw. The pieces are then bonded to electrodes on both their hot and cold sides by Sn-based brazing material, and at the same time the electrodes are bonded to pieces of ceramic with silver paste. The entire module is then placed inside a tube furnace and heated up to 563 K for 30 minutes to completely to fix the legs and electrodes. Copper wires are soldered onto the cold-side electrodes for 4-point current and voltage measurements. A Mini PEM (Advance Riko) is used for the evaluation of thermoelectric conversion efficiency (η). The electrical output power (P) and output heat flow (Q_{out}) of the thermoelectric module are measured under vacuum (< 5×10^{-2} mbar). A graphite sheet of 0.1 mm thickness and thermal silicone grease (ST1002, Slont) are used between the ceramic plate and the heater to reduce the thermal contact resistance. Good thermal contact was maintained using 60N compression springs. The hot-side temperature (T_{hot}) of the thermoelectric element is varied from 323 K to 548 K, whereas the cold-side temperature (T_{cold}) was maintained at about 293 K. A home-made device is used to characterize the cooling performance. The hot-side temperature of the module is controlled by the Cu heat sink connected to a thermostat (Lauda Ecoline RE106) with water-glycol cooling fluid. The T_{cold} and T_{hot} are measured by Pt100 thin-film resistance temperature detectors attached to the cold side and hot side of module, respectively. Readout of the Pt100 thin-film resistance temperature detectors is performed with a Multimeter (Keithley 2700 Data Acquisition System) with a Multiplexer (Keithley 7700 Differential-Multiplexer-Module). The current of 0 - 8 A is provided by a power source (Agilent E3644A). For measurements, the power source and data acquisition system were remotely controlled by a python script to

automatically perform measurements. The cooling characterization is performed in a high vacuum of ~10^{-7} mbar. Thermal insulation fibers are used to minimize radiative heat transfer between hot and cold side of the module. Note that only the cooling ΔT can be evaluated for the current device setup. Another important quantity of a cooler, the coefficient of performance (*COP*), will be evaluated in future works after installing a heat-flux sensor and heater.

Thermal cycling test

The robustness of the thermoelectric module against temperature cycling is evaluated in an argon-filled glovebox by a home-made setup. One side of the thermoelectric module is heated using a heat source of 50-225 °C and the other side is cooled using a heat sink of 15 °C. The heating and cooling rate of hot side is ~ 87 K/min and ~ 25 K/min, respectively. The internal resistance (R_{in}) of the thermoelectric module is evaluated by four-wire measurement after each cycle when the hot side temperature is at its low point of 50 °C.

Finite element simulation

COMSOL Multiphysics with Heat Transfer Module is used to perform the three-dimensional finite-element simulations of the power-generation characteristics for the thermoelectric module. A geometrical model with the same dimensions as the experimental thermoelectric element is used to calculate the electric power and heat flow outputs. The temperature-dependent Seebeck coefficient, electrical conductivity, and thermal conductivity for both *n*- and *p*-type materials are taken from the measured data as material properties in the simulations, while those for Cu interconnecting electrodes and the insulating AlN substrate are taken from material library in COMSOL. The electrical contact resistance of *n*- and *p*-type leg with the value of 26.6 μOhm cm^2 and 6 μOhm cm^2, respectively, are considered in the simulation model. The thermal contact resistance and radiation effects are not considered in the simulation model.

II. X-ray diffraction patterns

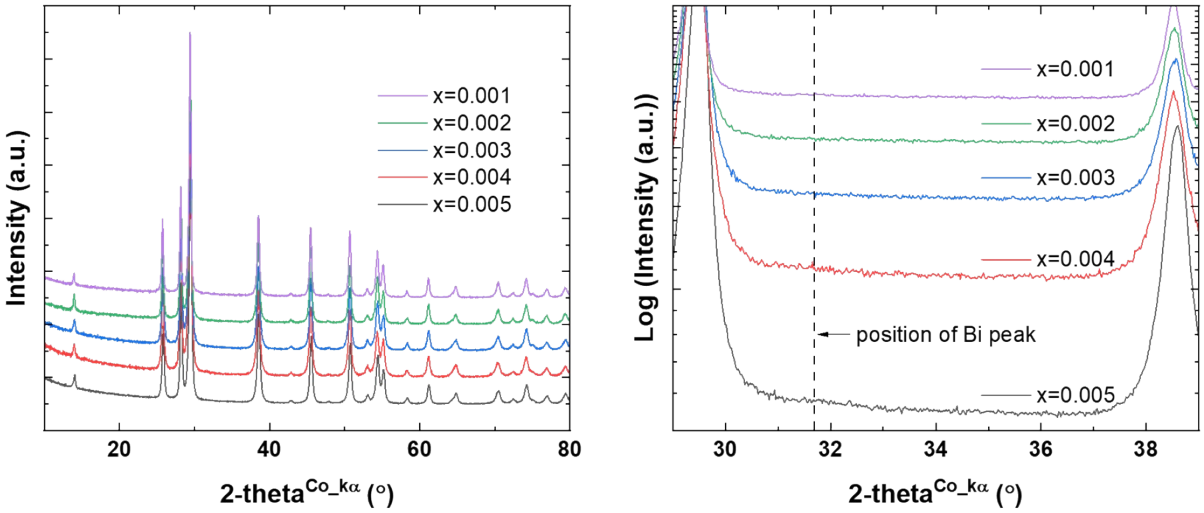

Figure S1. (Left) The x-ray diffraction patterns of $Mg_{3.6}Y_xSb_{0.6}Bi_{1.4}$ with x=0.001, 0.002, 0.003, 0.004, and 0.005. (Right) The enlarged view of Left, showing there is no presence of Bi peak. Note that the intensity is in log scale, which can display the minority peaks more prominently.

III. Temperature-dependent carrier concentration

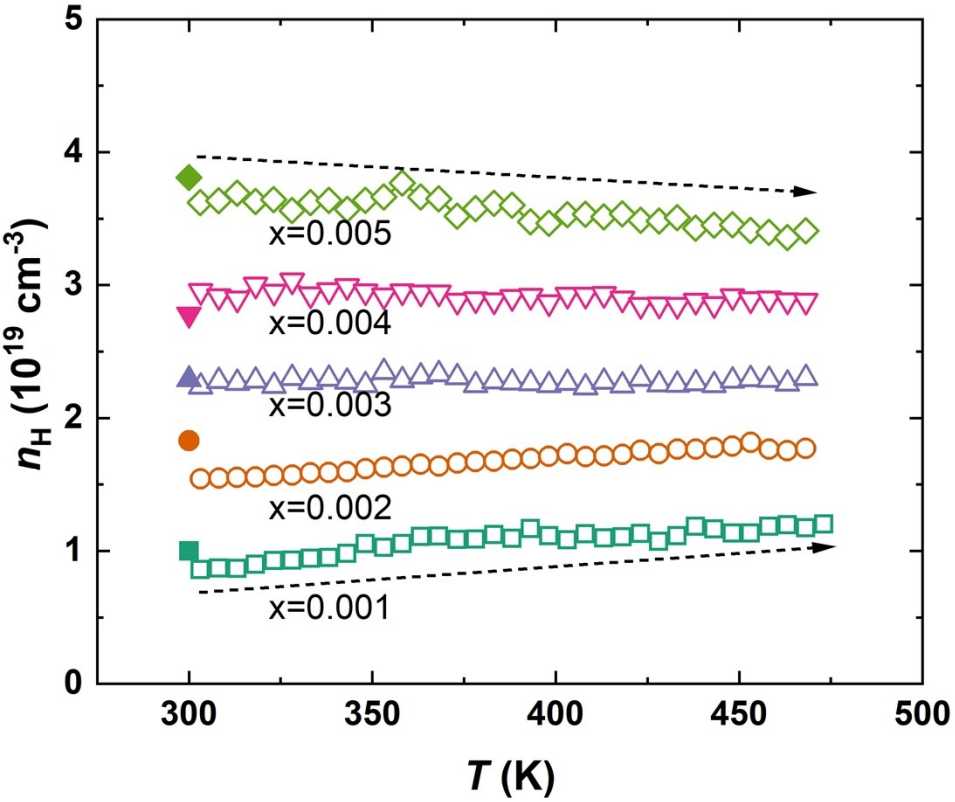

Figure S2. Hall carrier concentration from 300 K to 473 K of $Mg_{3.6}Y_xSb_{0.6}Bi_{1.4}$. The solid data points are measured at 300 K using PPMS.

IV. Effective masses and valley degeneracy

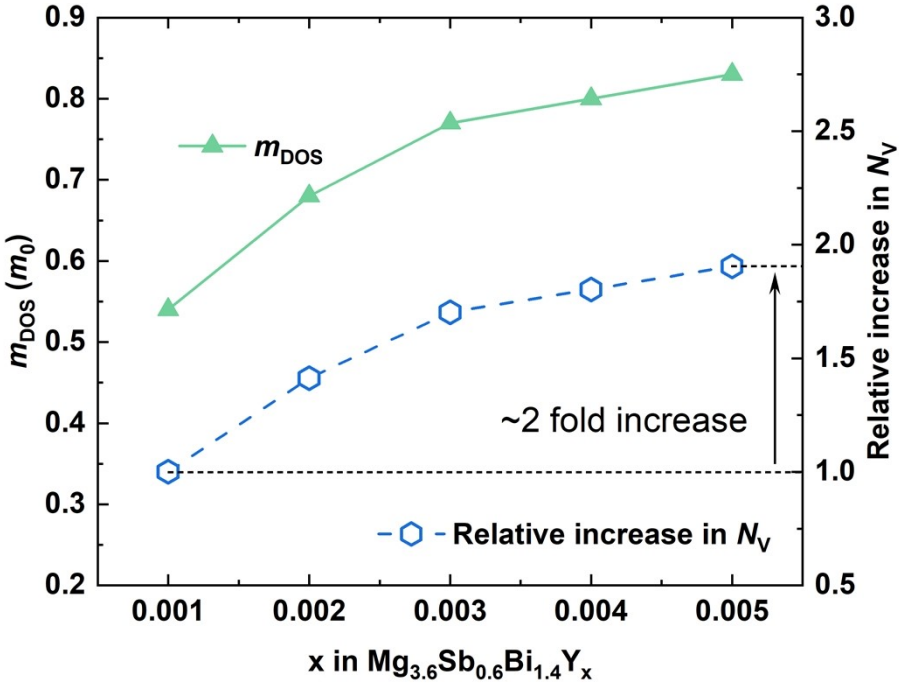

Figure S3. (Left) The density-of-state effective masses of $Mg_{3.6}Y_xSb_{0.6}Bi_{1.4}$ according to the Pisarenko relation. (Right) The estimated relative increase in N_V with respect to $Mg_{3.6}Y_{0.001}Sb_{0.6}Bi_{1.4}$ assumed that the band effective mass does not change with the doping level.

V. Thermoelectric properties of *p*-type $MgAg_{0.97}Sb_{0.99}$ and *n*-type $Mg_{3.6}Y_{0.003}Sb_{0.6}Bi_{1.4}$

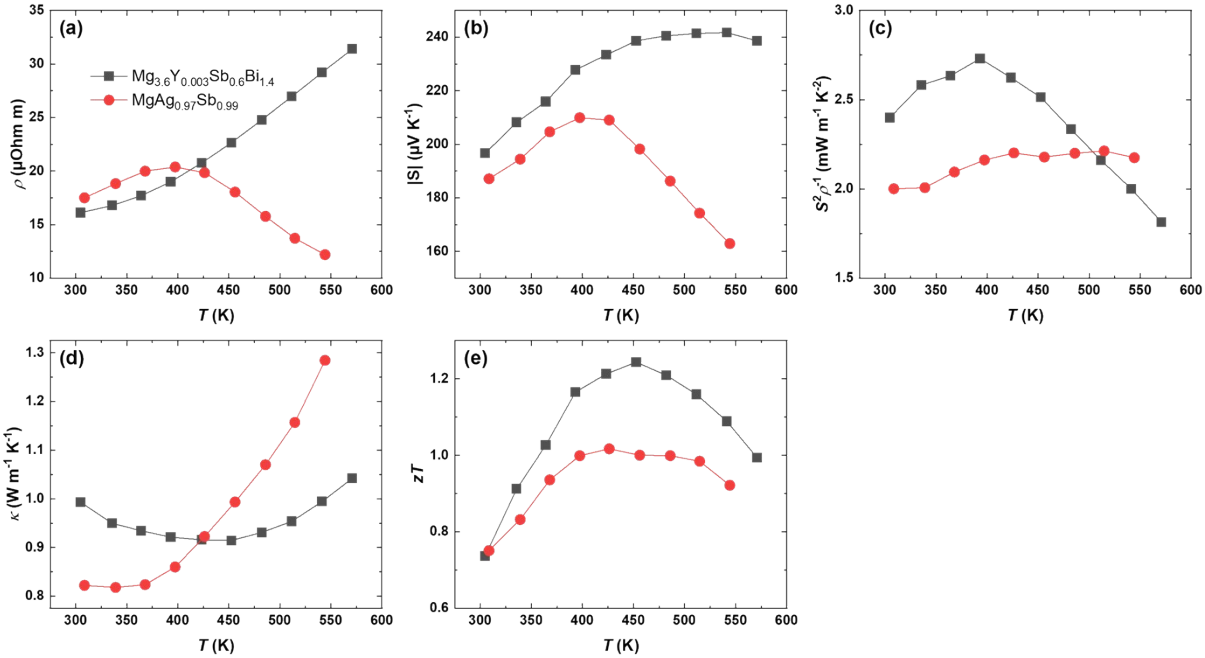

Figure S4. Temperature-dependent (a) electrical resistivity, (b) absolute Seebeck coefficient, (c) power factor, (d) thermal conductivity, and (e) *zT* of *p*-type $MgAg_{0.97}Sb_{0.99}$ and *n*-type $Mg_{3.6}Y_{0.003}Sb_{0.6}Bi_{1.4}$.

VI. Elemental mapping across the TE and the contact materials

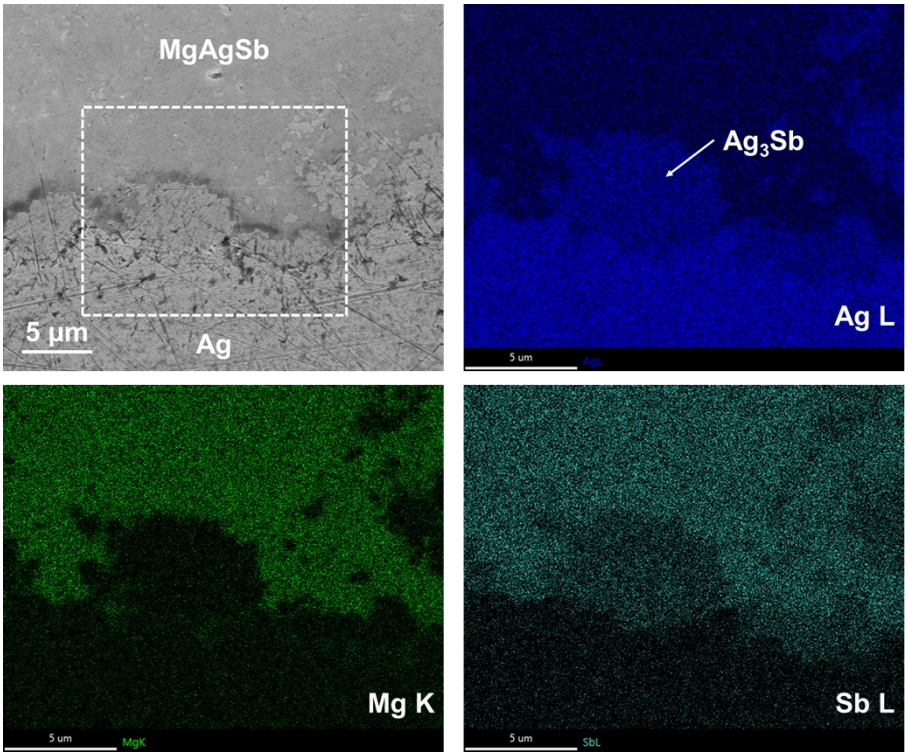

Figure S5. SEM-EDX elemental distribution across the junction of MgAgSb/Ag.

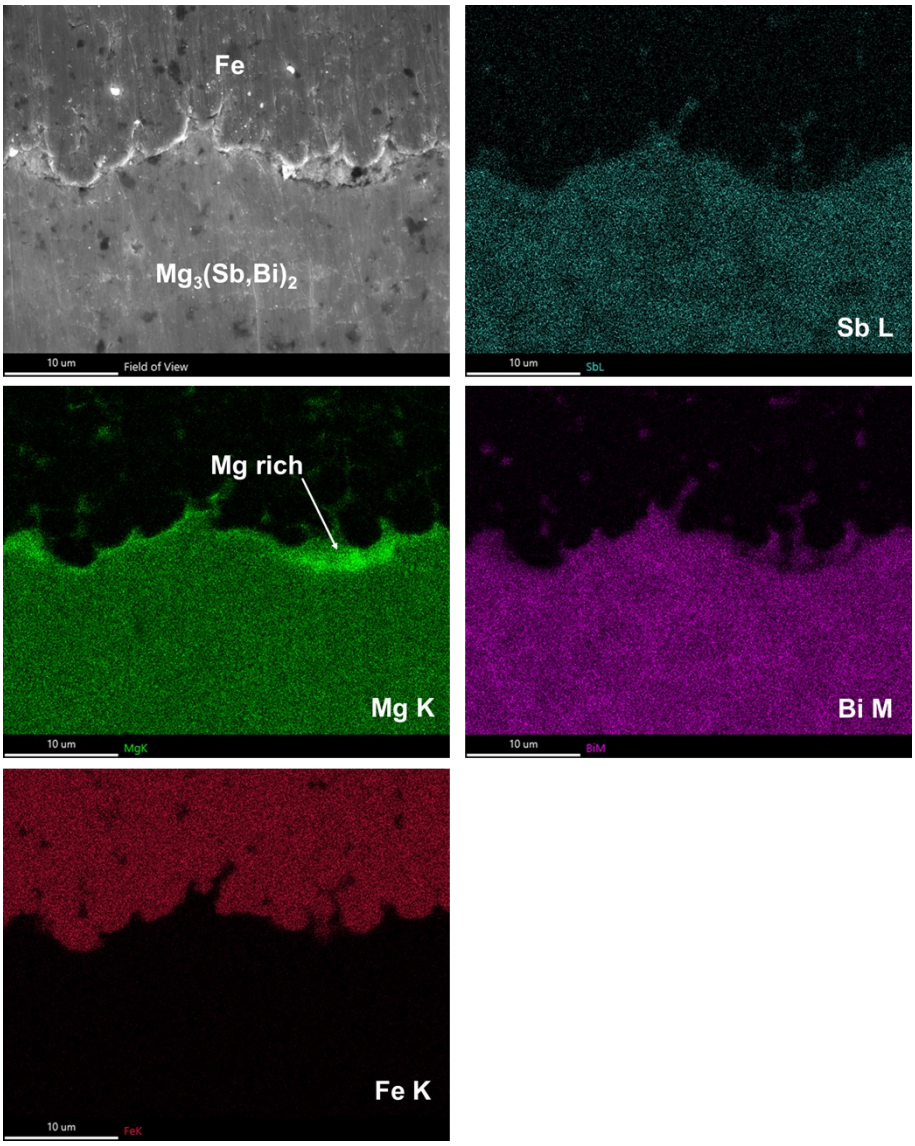

Figure S6. SEM-EDX elemental distribution across the junction of $Mg_3(Sb,Bi)_2$/Fe.

VII. Internal resistance and open circuit voltage

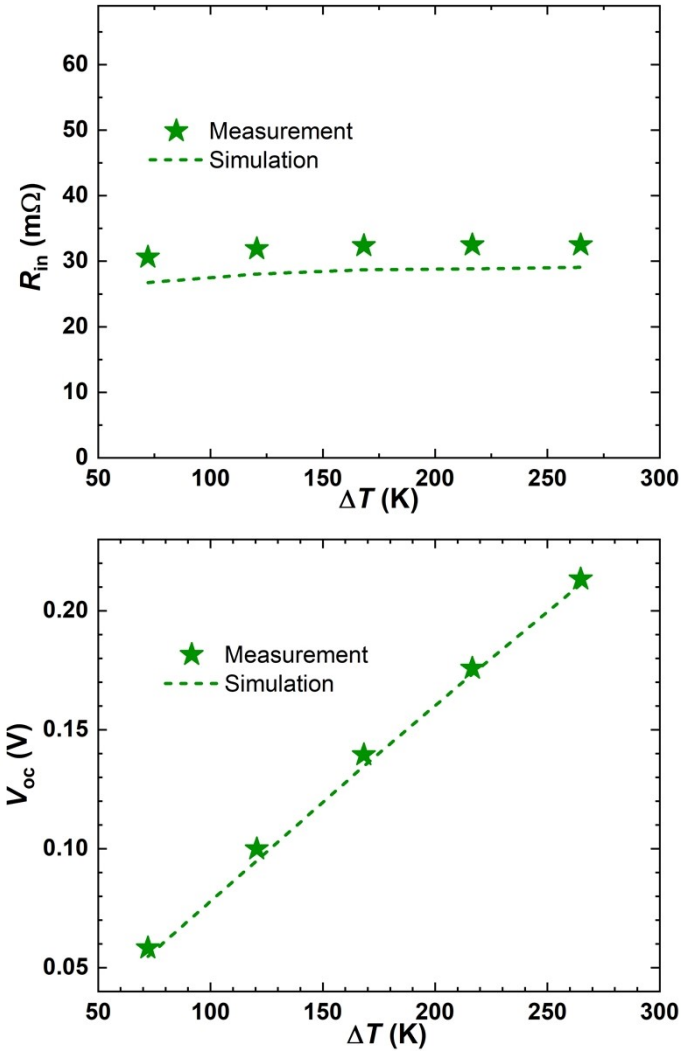

Figure S7. The (upper) internal resistance and (lower) open circuit voltage with respect to a series of temperature differences for a power generator.

VIII. Heat flow of the power-generation module

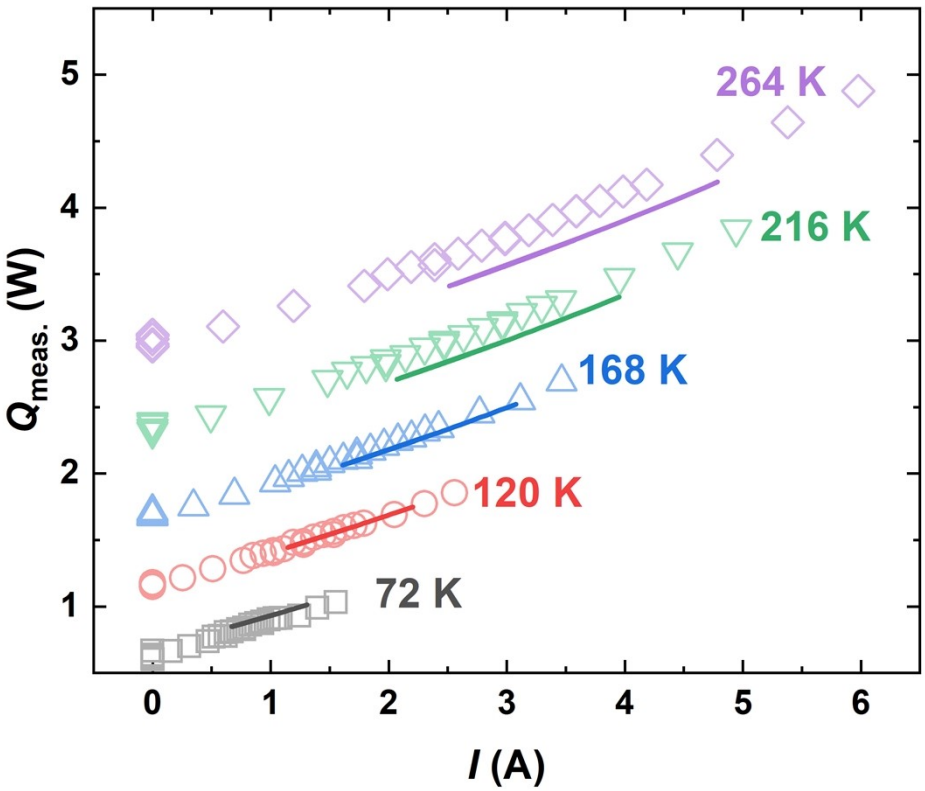

Figure S8. Current-dependent heat flow under a series of temperature differences. The solid lines are the simulated results.

IX. Temperature distribution of modules

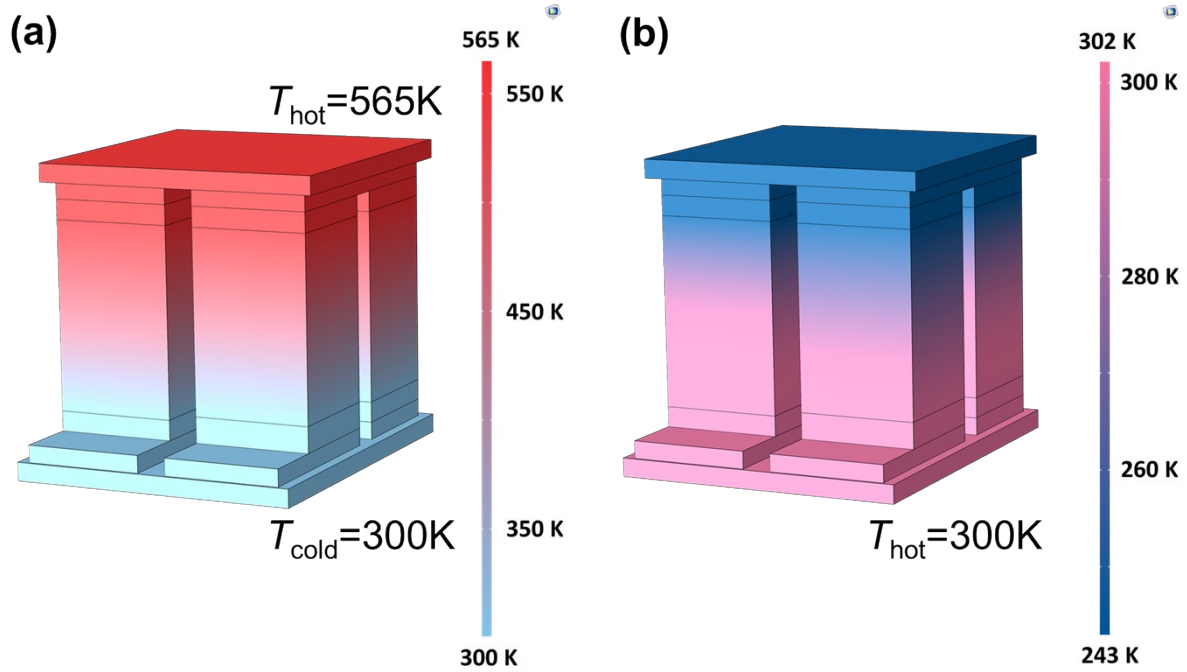

Figure S9. The temperature distribution of the module in working modes of (a) power generation and (b) cooling.

References

1. H. Zhao, J. Sui, Z. Tang, Y. Lan, Q. Jie, D. Kraemer, K. McEnaney, A. Guloy, G. Chen and Z. Ren, *Nano Energy*, 2014, **7**, 97-103.
2. M. T. Agne, K. Imasato, S. Anand, K. Lee, S. K. Bux, A. Zevalkink, A. J. E. Rettie, D. Y. Chung, M. G. Kanatzidis and G. J. Snyder, *Materials Today Physics*, 2018, **6**, 83-88.